

INTERCONNECTED PLASMONIC NANOGAP ANTENNAS FOR SUB-BANDGAP PHOTODETECTION VIA HOT CARRIER INJECTION

John Grasso*

Chemical and Biomolecular Engineering, University of Connecticut 191 Auditorium Road, Storrs, CT 06269, United States <u>John.grasso@uconn.edu</u>

Rahul Raman

Chemical and Biomolecular Engineering, University of Connecticut 191 Auditorium Road, Storrs, CT 06269, United States Rahul.raman@uconn.edu

Brian G. Willis

Chemical and Biomolecular Engineering, University of Connecticut 191 Auditorium Road, Storrs, CT 06269, United States Brian.willis@uconn.edu

> Received Day Month Year Revised Day Month Year

Modern integrated circuits have active components on the order of nanometers; however, optical devices are often limited by diffraction effects with dimensions measured in wavelengths. Nanoscale photodetectors capable of converting light into electrical signals are necessary for the miniaturization of optoelectronic applications. Strong coupling of light and free electrons in plasmonic nanostructures overcomes these limitations by confining light into sub-wavelength volumes with intense local electric fields. Localized electric fields are intensified at nanorod ends and in nanogap regions between nanostructures. Hot carriers generated within these high field regions from nonradiative decay of surface plasmons can be injected into the conduction band of adjacent semiconductors, enabling sub-bandgap photodetection. The optical properties of these plasmonic photodetectors can be tuned by modifying antenna materials and geometric parameters like size, thickness, and shape. Electrical interconnects provide connectivity to convert light into electrical signals. In this work, interconnected nanogap antennas fabricated with 35 nm gaps are encapsulated with ALD deposited TiO_2 , enabling photodetection via Schottky barrier junctions. Photodetectors with high responsivity (12 μ A/mW) are presented for wavelengths below the bandgap of TiO_2 (3.2 eV). These plasmonic nanogap antennas are subwavelength, tunable photodetectors with sub-bandgap responsivity for a broad spectral range.

Keywords: Plasmonic dimers; nanofabrication; Schottky; photodetector; localized surface plasmon resonance

1. Introduction

Modern nanophotonics has flourished due to plasmonics, yielding tremendous developments in various interdisciplinary fields by harnessing favorable light-matter interactions.¹ Plasmonic metal (Ag, Au, Cu) nanostructures can produce localized surface plasmons (LSPs) upon illumination with light from electrons reaching higher energy states

via photoexcitation.² Primary effects from generation of LSPs are local electromagnetic (EM) enhancements and hot carrier production.² Hot carrier generation (high energy electrons/holes emanating from electronic excitation decay) is proportional to EM enhancements and has been successfully used in photocatalytic applications as a method to reduce activation energy and alter selectivity towards favorable products.^{3,4} Plasmonic nanostructures may exhibit resonances that can be tuned by altering composition, geometry, and spatial configurations resulting in control of wavelengths where maximum plasmonic effects occur.² Further EM field enhancement occurs when plasmonic nanostructures are arranged as dimers that create hotspots for hot carrier generation. Localized electric fields are intensified in nanogap regions between nanostructures where enhancements can reach over 1000.² These nanogap regions enhance hot carrier formation and there is an inverse relationship between nanogap size and hot carrier generation rates.² Another advantage of using dimer pairs is that they have large extinction cross sections and act as antennas to increase light collection. Plasmonic dimers can be electrically connected for electro-optic applications such as photodetectors.⁵

Photodetection is possible using internal photoemission at Schottky barriers where photoexcited carriers transfer from metal to a semiconductor material through an interface. 6.7 The Schottky barrier may be lower in energy compared to the semiconductor material bandgap, which enables sub-bandgap photodetection due to the lower energy required to promote charge carriers into the conduction band. By integrating Schottky diodes with plasmonic nanostructures, photodetection can occur over a large wavelength range by collecting hot carriers. Hecht et al. recently measured the responsivity of a pair of Au plasmonic nanostructures contacting TiO₂ semiconductor layers with a Au/TiO₂ Schottky barrier around 1 eV.9 The structures were fabricated as single devices through focused ion beam milling which has limitations for large array fabrication due to lower throughput compared to electron-beam lithography. Halas et al. measured the responsivity of gold nanorod arrays on Si and measured a Schottky barrier of 0.5 eV, which is half of the barrier reported for TiO2.8 Baumberg et al. studied photocurrent detection through quantum tunneling with gold nanospheres and observed responsivities in the range of 0.01 μA/mW.¹⁰ In this study, we evaluate the responsivity and detectivity of plasmonic photodetectors formed using arrays of interconnected dimers with Au/TiO₂ Schottky barriers. We measure photocurrents at different bias voltages, optical wavelengths, polarization directions, and analyze optical extinction data pre- and post-TiO₂ deposition.

2. Experimental

Nanostructures were fabricated using an Elionix BODEN 150 electron beam writer on a fused silica wafer with poly (methyl methacrylate) (PMMA) photoresist and a layer of Espacer. Samples were developed using a methyl isobutyl ketone (MIBK) and isopropanol (IPA) mixture followed by an O₂ plasma descum treatment of 75 W for 30 seconds. Metal was deposited in an electron beam evaporator with 4 nm Ti and 45 nm Au. Remover PG was used for lift-off processing. A second lithography step was used to add bonding pads and electrical connections to nanostructures. Shipley 1805 and LOR 3A resists were

applied followed by exposure with a Heidelberg MLA-150 maskless aligner tool. Metal deposition was performed again to deposit 10 nm Ti and 200 nm Au contacts followed by lift-off processing with Remover PG. A third lithography step was used with Shipley 1805 and LOR 3A resists and the MLA-150 tool to create openings around the photodetectors for atomic layer deposition (ALD) of the semiconductor layers. A Savanah ALD system was used to deposit Al₂O₃ and TiO₂ on samples at 150°C with water co-reactant and trimethyl aluminum (TMA) and tetrakis(dimethylamino) titanium (TDMAT) used as precursors, respectively. Another lift-off step was used to remove the ALD coated photoresist leaving TiO₂ only on the device regions. Optical extinction curves were measured using an ellipsometer set in polarized transmission mode to measure LSP intensity. Scanning electron microscopy (SEM) was used to image nanostructures using a 4 nm layer of a sputter-deposited Au/Pd target to assist in charge dissipation. PROSEM software (Genisys) was used to analyze high-resolution SEM images to measure nanostructure dimensions.

A Keithley 2612B SMU was used to measure photocurrents and device I-V characteristics in the dark. Photodetection experiments were performed at various bias voltages, spanning 1 to 3.5 V. The device was blocked from light with a shutter for 30 seconds followed by cycles of exposure to light for 5 seconds and blocking for 10 seconds. Edmund Optics 50 nm band pass filters and an Edmund Optics wire grid VIS-NIR polarizing film were used to measure wavelength and polarization dependence, respectively. The power from the light source for each stage of testing was measured with a Newport 843-R power meter. Dark currents are subtracted using a baseline correction algorithm to record photocurrents as changes in current upon illumination.

3. Results and Discussion

3.1. Plasmonic Nanostructure Design

Figure 1 illustrates the design of interconnected plasmonic nanogap photodetectors. Device areas are 25x25 um² regions with arrays of nanostructures contacted by Au lines. Photodetectors consist of nanorod dimers with bisecting interconnect lines encapsulated in ALD TiO₂. Prior work with interconnected nanogap antennas guided geometric parameters to minimize perturbations to dimer resonance, as well as tuning plasmonic resonances around 800 nm. ^{5,11,12} Twelve cycles of ALD Al₂O₃ were deposited prior to TiO₂ layers as thin insulating layers to reduce dark currents and improve rectifying characteristics. ⁹ Titania (TiO₂) film thickness is measured as 45.7 nm via spectroscopic ellipsometry using a flat Si wafer included in the ALD run. Previous work suggests that as-deposited TiO₂ at 150 °C from TDMAT and water results in amorphous thin films, verified by grazing incidence X-ray diffraction (GIXRD). ¹³ Energy dispersive X-ray analysis (EDAX) was used to perform elemental mapping of photodetectors. Figure 1(c) confirms the selective deposition of TiO₂, which covers the nanostructure regions. Faint traces of titanium are also detected on the Au contact lines due to the Ti adhesion layers applied during metal deposition, but they are unrelated to the ALD TiO₂.

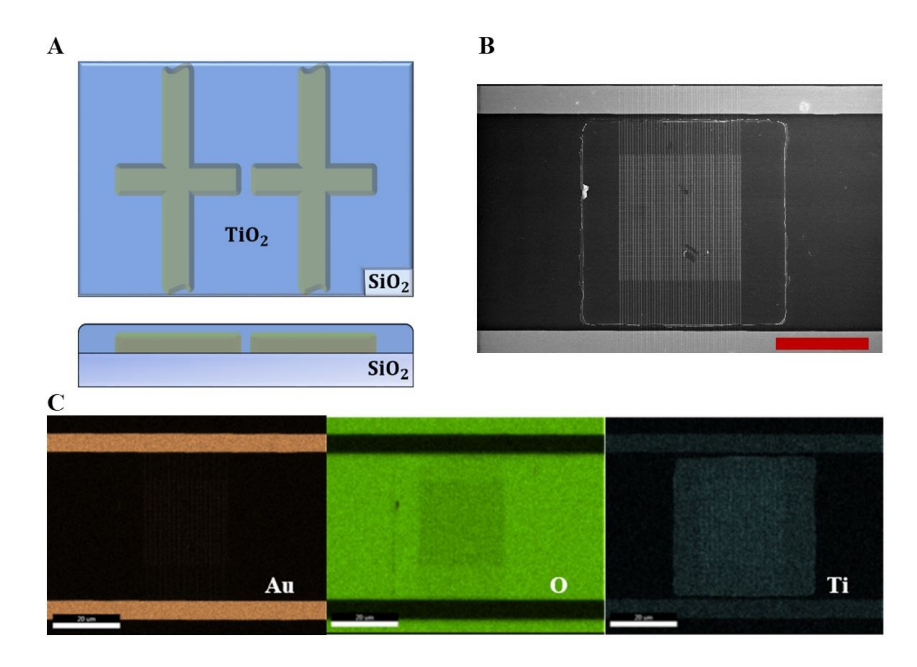


Figure 1: Interconnected plasmonic dimers are coated with TiO_2 via ALD at 150 C. (A) Simplified schematic of plasmonic photodetectors within unit cell; top and side views. (B) SEM image of plasmonic array post-ALD. Scale bar is 30 μ m. (C) EDAX elemental mapping analysis images for Au, O, and Ti.

Optical extinction spectra were investigated for samples before and after ALD TiO₂, shown in Figure 2. The uncoated antennas show a strong dipole resonance at 800 nm (blue line). There is a smaller peak near 530 nm assigned to the interconnect lines. ¹⁴ After ALD TiO₂, the surface plasmon resonance peak red shifts from 800 to beyond 1000 nm. This shift is expected due to the increased refractive index (2.39 @ 623.8 nm) for the surrounding medium (TiO₂) and is well understood in literature. ^{2,15} High-resolution SEM images were used to extract geometric parameters of fabricated nanostructures and verify conformal ALD coatings. Figure 3(a) depicts bare nanostructures before ALD; average nanorod lengths and widths were 134.2 ± 9.5 nm and 53.6 ± 0.8 nm, respectively. Average nanogap distance was 33.6 ± 6.7 nm. Nanostructures were successfully encapsulated in TiO₂, as shown in Figure 3(b). The TiO₂ layers fill in the nanogaps to create Au/TiO₂/Au plasmonic junctions. Further investigation is required to characterize how TiO₂ deposition conditions and film thickness affect plasmon resonances and subsequent photoresponses.

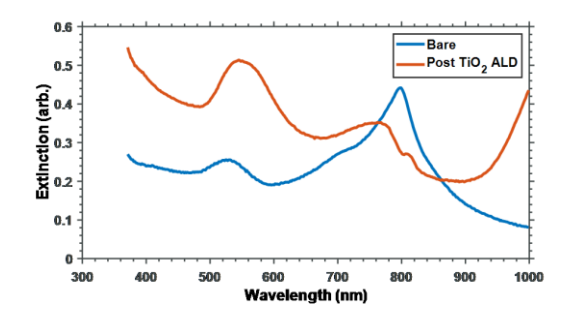


Figure 2: Experimental extinction spectra pre- and post- TiO₂ ALD at 150 C.

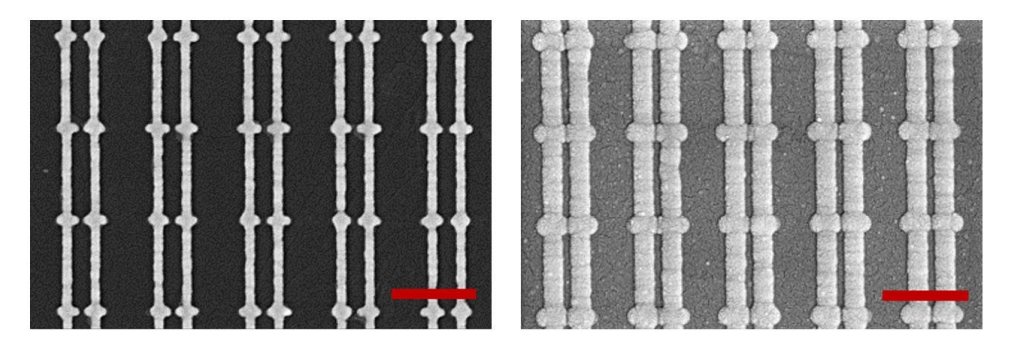


Figure 3: SEM images of plasmonic nanostructures. (Left) as-fabricated, before ALD. (Right) post-ALD of TiO₂ at 150 C. Scale bar is 500 nm.

3.2. Electrical Characteristics

Current-voltage (I-V) characteristics of Au/TiO₂ Schottky barrier junctions at several temperatures ranging from 10 – 30 °C are given in Figure 4(a). The metal-semiconductor-metal (MSM) structures feature two Schottky barriers connected in series. Under voltage bias conditions, one diode is forward biased and the other is reverse biased; thus, the photodetectors exhibit symmetric I-V behavior for both bias conditions. At low to moderate bias voltages, current flow is governed by the Schottky contact under reverse bias. Image force lowering, or the Schottky effect, and tunneling currents contribute to current in these regimes. ¹⁶ For sufficiently large bias voltages, the forward biased Schottky contact in the MSM structure dominates current flow and can be modeled according to thermionic emission theory, as follows: ¹⁶⁻²⁰

$$I = AA^*T^2 \exp\left(-\frac{\Phi_B}{k_B T}\right) \left[\exp\left(\frac{q(V - IR_s)}{nk_B T}\right) - 1\right]$$
 (1)

where A is the effective diode area (cm²), A* is the effective Richardson constant for TiO₂ (1200 A/cm²/K²)²¹, k_B is the Boltzmann constant, q is electronic charge, V is applied bias, Φ_B is the Schottky barrier height (eV), n is an ideality factor, and R_s is series resistance in ohms. Electronic properties of Schottky contacts are characterized by barrier height and ideality factor. Other properties, such as series resistance, also play an important role in

determining device performance, thus accurate parameters are crucial for effective device design. Methods which rely on extrapolation of the linear region of ln (I) – V curves may introduce uncertainty in parameter estimation due to considerable deviation from linearity at sufficiently large applied voltages, caused by series resistance. ¹⁸ Alternatively, barrier height, ideality factor, and series resistance can be determined by a method pioneered by Cheung et al. ¹⁷ Figure 4(b) depicts the current modeled according to parameters calculated from the Cheung method. The model is in good agreement with the experimental I-V characteristics, especially at large applied voltages, suggesting thermionic emission is the dominant transport mechanism in this region.

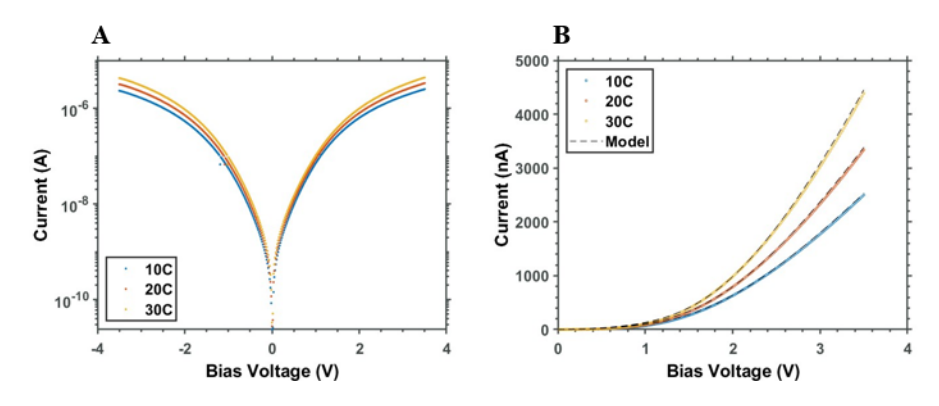


Figure 4: I-V current characteristics of plasmonic photodetector at several temperature ranges. (a) ln(I) for positive and negative applied bias. (b) thermionic emission current modeled with extracted Schottky diode parameters from Cheung method.

Using the Cheung method, barrier height, ideality factor, and series resistance are estimated as 0.75 eV, 15.6, and 256 kΩ at 30 °C, respectively. The estimated barrier height is lower than the theoretical barrier (1.0 eV) for Au/TiO₂ and may be a result of the TiO₂ film quality and Au interface. Amorphous TiO₂ exhibits increased conductivity attributed to its electronically defective nature, which would lead to increased leakage current and non-ideality.²² Additionally, trap states at the interface could shift the fermi level towards the conduction band, resulting in lowered barrier heights. 19 An ideality factor greater than 1 suggests deviation from ideal thermionic emission current. Several factors can contribute to n being greater than unity, including: the presence of an interfacial layer,²³ trap states in the band gap, barrier height inhomogeneity^{21,24,25} and increased contribution from other current mechanisms, such as Fowler-Nordheim tunneling and generation-recombination currents within the depletion region. 19 Series resistance is related to the bulk resistivity of TiO₂ and also increases with insulating layers between the metal and semiconductor, such as Al₂O₃. Large deviations may additionally be a result of discontinuity in TiO₂/Al₂O₃/Au interface, and/or impurities in the TiO₂ film. Post-deposition annealing to promote amorphous-to-crystalline phase transition may improve Schottky diode characteristics.

3.3. Photodetection

Photocurrent measurements were performed with excitation wavelengths from 300 nm to 2800 nm using a fiber-coupled tungsten-halogen light source (ThorLabs, SLS201L). The fiber source is collimated and focused onto a sample with a spot diameter of 0.72 mm and light power of 2.4 mW. Photocurrents were measured while varying applied bias, spanning from 1.5 to 3.5 V. Responsivity (R) and specific detectivity (D^*) were calculated as photodetector metrics, according to the following equations:⁹

$$R = \frac{l_{ph}}{P} \left(\frac{A_{beam}}{A_{eff}} \right)$$

$$D^* = \frac{A_{eff}R}{\sqrt{2qI_D}}$$
(2)

$$D^* = \frac{A_{eff}R}{\sqrt{2qI_D}} \tag{3}$$

where Iph is the photocurrent, Abeam is the area of the light beam, Aeff is the effective Au/TiO₂ contact area of the photodetector (6.8e-10 m²), P is light power, and I_D is dark current. Figure 5(a) illustrates time dependent photo response data, demonstrating square wave responses upon illumination. Figure 5(b) shows an increase in both responsivity and specific detectivity as applied bias increases. Responsivity of 10⁻³ A/W and specific detectivity of 10⁵ Jones for the plasmonic nanogap arrays show three and two orders of magnitude enhancement compared to single nanogap antennas of similar design, respectively. Similarly, there is a 1000x improvement of responsivity compared to nanorod arrays on n-Si.8 Dark currents increase with larger bias voltages; however, decreased detectivity is not observed due to the offsetting increase in responsivity, see Equation (3).

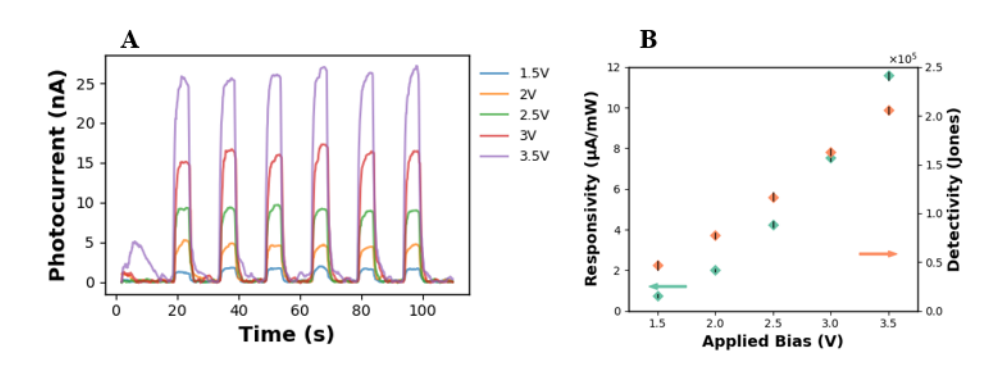


Figure 5: Comparison of photocurrent as a function of applied bias. (A) Time dependence of the photocurrent at 1.5 – 3.5 V voltage bias. (B) Responsivity; left axis, and detectivity; right axis, photodetector metrics. Error bars correspond to standard error of 6 repeated measurements.

Previous studies of plasmonic junctions used monochromatic light from a white light laser, but quartz tungsten halogen sources contain a small proportion of photons with energy sufficient to transverse the intrinsic bandgap of TiO₂ (3.2-3.4 eV), ¹³ which may

contribute to photocurrent via the photoelectric effect. To ensure photocurrents are produced via internal photoemission, the wavelength dependency of responsivity was investigated. Wavelength dependence was studied with the use of 50 nm bandpass filters ranging from 700 nm – 1100 nm. Power readings were measured for each filter. Figure 6(a) confirms sub-bandgap photodetection was achieved and responsivity values are consistently greater than 8 μ A/mW. The photon energy of NIR light is sufficiently below the expected band gap of TiO₂ to support a mechanism involving photocurrent generation via photoemission of electrons from the Au contacts into the TiO₂ semiconductor layer. Similar responsivity was observed with filters compared to the white light spectrum. External quantum efficiency (EQE) is calculated (EQE (%) = [R_{\(\text{L}\)E_{\(\text{I}\)}/q]x100) based on responsivity and photon energy (E_{\(\text{L}\)}) at the central wavelength (\(\text{L}\)) for each optical filter. Quantum efficiency is between 1.1 – 1.8% for all wavelengths. This is significantly larger than previous reports of single nanogap antenna pairs with photodetectors exhibiting 0.01% EQE.⁹}

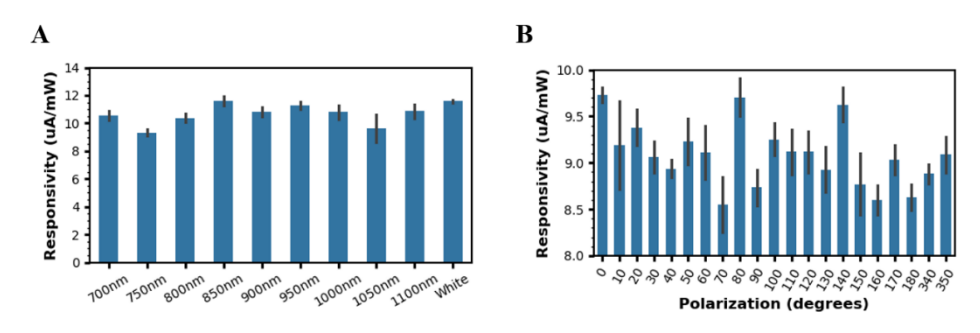


Figure 6: (A) Wavelength and (B) polarization responsivity dependence at 3.5V applied bias. Error bars represent standard error of 6 repeated measurements.

Photocurrents generated from hot carriers are expected to increase at resonance, but this effect is not clearly evident in Figure 6(A). One possible explanation that a stronger wavelength dependence is not observed is because the resonance wavelength is shifted beyond the range of this investigation. Figure 2 shows that the extinction is increasing beyond 1000 nm. Additionally, the large bandwidths of optical filters (50 nm) may smear the response and be too broad to detect any wavelength dependency on photoresponses. Further study with different nanostructure designs is needed to elucidate wavelength dependent photocurrents corresponding to plasmonic resonances.

In addition to wavelength effects, light polarization is also expected to influence hot carrier generation through the polarization dependence of the plasmon resonances. Photocurrent experiments were conducted using white light and a NIR polarizing filter to investigate how polarization affects responsivity, depicted in Figure 6(b). For nanorods, theory indicates the greatest EM field enhancement occurs for light polarized parallel to the longitudinal dimensions of the rods in the direction of the nanogaps. Maximum responsivity, 9.7 μ A/mW, is observed for polarization angle of 0 degrees relative to longitudinal axis. Increasing the angle towards the transverse direction is accompanied by

a decrease in responsivity, which is consistent with expectations. The data are scattered and the trend is not smooth, but the variation in photocurrents with polarization axis hints at plasmonic influences on photoemission of electrons from the metal into the semiconductor.

4. Conclusions

Arrays of nanofabricated plasmonic dimers with interconnects were coated with TiO₂ by ALD to study sub-bandgap photodetection with Au/TiO₂/Au Schottky barrier nanojunctions. Non-linear I-V characteristics support the formation of Schottky barriers and a photocurrent mechanism where photo-excited electrons are injected into the semiconductor layer. Estimation of Schottky barrier heights and ideality factors suggest non-ideal behavior, especially at low voltage biases, which may be attributed to TiO₂ trap states, barrier height inhomogeneity, insulating layers, and/or amorphous crystallinity. Nonetheless, high responsivities of 12 μA/mW and detectivities of 2.1e5 Jones demonstrate three orders of magnitude improvement compared to similar plasmonic photodetectors. Further optimization of device designs, materials, and process engineering may lead to a new class of nanoscale photodetectors based on plasmonic nanojunctions.

Acknowledgements

The authors acknowledge the National Science Foundation (NSF) (Grant No. 2150158) and the Office of Naval Research (Grant No. N00014-22-1-2567). This work was performed in part at the Harvard University Center for Nanoscale Systems (CNS); a member of the National Nanotechnology Coordinated Infrastructure Network (NNCI), which is supported by the National Science Foundation under NSF award no. ECCS-2025158. Electron microscopy was performed at the UConn/Thermo Fisher Scientific Center for advanced Microscopy and Materials Analysis (CAMMA).

References

- 1. J. Tang, Q. Guo, Y. Wu, J. Ge, S. Zhang and H. Xu, ACSNano 18, 4 (2024).
- G. Baffou, Thermoplasmonics: Heating metal nanoparticles using light, (Cambridge University Press, Cambridge, 2018).
- 3. J. Fojt, T. P. Rossi, P. V. Kumar and P. Erhart, ACSNano 18, 8 (2024).
- 4. Y. Yuan, L. Zhou, H. Robatjazi, J. L. Bao, J. Zhou, L. Yuan, M. Lou, M. Lou, S. Khatiwada, E. A. Carter, P. Nordlander and N. J. Halas, *Science*, 378, 6622 (2022).
- R. Raman, J. Grasso, and B. G. Willis, International Journal of High Speed Electronics and Systems, 32 (2023).
- 6. R. T. Tung, Appl. Phys. Rev., 1 (2014).
- 7. Y. Lao and A. Perera, Advances in OptoElectronics 16 (2015).
- 8. M. Knight, H. Sobhani, P. Nordlander and N. Halas, Science 332, 6030 (2011).
- P. Pertsch, R. Kullock, V. Gabriel, L. Zurak, M. Emmerling and B. Hecht, Nano Letters, 22, 17 (2022).
- 10. D. Kos, D. R. Assumpcao, C. Guo and J. J. Baumberg, ACSNano 15, 9 (2021).
- 11. C. Zhang, T. Gao, D. Sheets, J. N. Hancock, J. Tresback and B. Willis, JVSTB 39, 5 (2021).

- 12. D. T. Zimmerman, B. D. Borst, C. J. Carrick, J. M. Lent, R. A. Wambold, G. J. Weisel and B. G. Willis, *J. Appl. Phys.* **123** (2018).
- R. Khan, H. Ali-Loytty, J. Saari, M. Valden, A. Tukianinen, K. Lahtonen and N. V. Tkachenko, Nanomaterials 10, 8 (2020).
- 14. B. G. Willis, J. Grasso, C. Zhang, and R. Raman, ACS Appl. Nano Mater. 6, 23 (2023).
- 15. P. K. Jain and M. A. El-Sayed, J. Phys. Chem. C 11, 47 (2007).
- 16. J. Fu, M. Hua, S. Ding, X. Chen, R. Wu, S. Liu, J. Han, C. Wang, H. Du, Y. Yang, and J. Yang, *Scientific Reports* 6 (2016).
- 17. S. K. Cheung and N. W. Cheune, Appl. Phys. Lett. 49, 2 (1986).
- 18. G. Guler, O. Gullu, S. Karatas and O. F. Bakkaloglu, J. Phys.: Conf. Ser. 153 (2009).
- M. A. Kadaoui, W. B. Bouiadjra, A. Saidane, S. Belahsene and A. Ramdane, Superlattices and Microstructures, 82 (2015).
- 20. C. D. Lien, F. C. T. So and M. A. Nicolet, IEEE Transactions of electron devices 31, 10 (1984).
- 21. G. Rawat, H. Kumar, Y. Kumar, C. Kumar and D. Somvanshi, *IEEE Electron Device Letters* **38**, 5 (2017).
- M. Hannula, H. Ali-Loytty, K. Lahtonen, E. Sarlin, J. Saari and M. Valden, *Chem. Mater.* 30, 4 (2018).
- 23. S. Chaliha, M. N. Borah, P. C. Sarmah and A. Rahman, Int. J. Thermophys. 31 (2010).
- 24. N. A. Al-Ahmadi, Heliyon 6 (2020).
- H. Altuntas, A. Bengi, U. Aydemir, T. Asar, S. S. Cetin, I. Kars, S. Altindal and S. Ozcelik, *Mater. Sci. Semicond. Process.* 12, 6 (2009).
- 26. N. Dharmale, S. Chaudhury, R. Mahamune and D. Dash, Mater. Res. Express 7 (2020).